

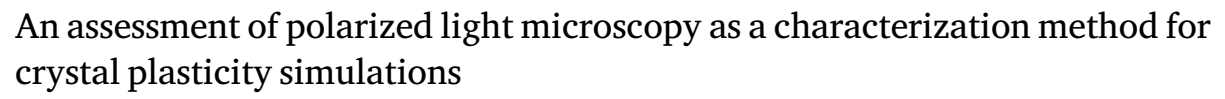
Contents lists available at ScienceDirect

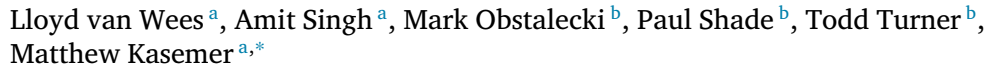
# Materialia

journal homepage: www.elsevier.com/locate/mtla



# Full length article





- a Department of Mechanical Engineering, The University of Alabama, Tuscaloosa, AL, 35487, United States of America
- b Air Force Research Laboratory, Materials and Manufacturing Directorate, Wright-Patterson AFB, OH 45433, United States of America

## ARTICLE INFO

# Keywords: Crystal plasticity finite element method Polarized light microscopy Material characterization HCP crystals Stress

## ABSTRACT

Polarized light microscopy is a large-area, high-resolution, high-throughput microstructural characterization method for polycrystalline materials comprised of hexagonal close-packed crystals. Due to the fact that polarized light microscopy only determines the orientation of a crystal's c axis, it is necessary to assess the applicability of this new characterization modality for use in integrated computational materials engineering workflows for simulating the deformation response of polycrystalline materials. We present a computational study in which the effect of this orientation ambiguity on the predictions of crystal plasticity finite element simulations is quantified. We focus on an idealized polycrystalline sample with random texture, from which a number of c axis-similar samples are generated, each with random rotations about each constituent crystal's c axis. We scrutinize the differences in stress field predictions between the reference sample and the randomly altered samples during monotonic tensile tests, as well as the spatial differences in predictions. Our findings indicate that differences are lowest in the elastic regime, and increase dramatically during the macroscopic elastic—plastic transition. We further find that results do not exhibit a strong spatial dependence, indicating that orientation and neighborhood are the primary causes of differences in stress field predictions.

## 1. Introduction

Modeling the deformation response of polycrystalline metals is of great interest for engineering component design, material processing design, and material design. Over the course of the last century, deformation modeling has progressed rapidly. Namely, the development of various mean-field approaches in the 1920s/1930s [1,2] provided upper- and lower-bounding limits to material behavior, while the development of self-consistent models from the 1960s [3] through the 1990s [4] provided more refined results considering some grain neighborhood effects. The development of full-field crystal plasticity finite element modeling (CPFEM) in the 1990s and early 2000s [5-7], however, has afforded researchers the most accurate predictions of the deformation response of polycrystalline aggregates to date. By explicitly considering high-fidelity representations of microstructures, as well as the anisotropic elastic and plastic deformation response of crystals (with varying degrees of complexity and physics considered), CPFEM represents the most accurate approach for deformation modeling at the scale of the polycrystal.

Modern integrated computational materials engineering (ICME) workflows rely on a wide range of experimental material characterization tools at various length scales to inform the construction of virtual polycrystals utilized in simulations [8-10]. Example uses of various methods at various length scales include: transmission electron microscopy (TEM) to characterize intragrain precipitate distributions [11-13]; scanning electron microscopy (SEM) and electron backscatter diffraction (EBSD) to characterize grain sizes and shapes in two dimensions, as well as crystallographic texture [14-16]; high energy X-ray diffraction (HEXRD) to characterize three-dimensional grain maps [17-19]. While TEM, SEM/EBSD, and HEXRD have each benefited in the past decades from great leaps in knowledge, technology, and software, they are still relatively esoteric methods that require highly skilled professionals to properly gather data, require expensive equipment, and are time-intensive for data collection and analysis. As modern ICME workflows demand increased throughput to facilitate modern challenges (e.g., material design), new material characterization modalities that offer promise to increase throughput (including ultrasonic [20-23] and optical methods) become increasingly attractive.

E-mail address: mkasemer@eng.ua.edu (M. Kasemer).

Corresponding author.

Regarding optical methods, polarized light microscopy (PLM) is particularly attractive as a surrogate for EBSD [24,25]. Overall, PLM provides sufficient resolution for materials science applications (especially at scales relevant to CPFEM simulations), though with data collection rates that far outpace EBSD. PLM as a characterization modality is not, however, without its limitations. First, PLM is suitable primarily for materials containing crystals exhibiting hexagonal close-packed symmetry. Second, PLM orientation measurement is most accurate when the sample possesses a wide range of crystallographic orientations, somewhat limiting the technique to weakly textured materials [25]. The final limitation is that PLM is able to determine only the orientation of the crystal's c axis, but not the rotation about the c axis [25,26]. In other words, there exists ambiguity in the crystallographic orientation of the crystals. While the first and second issues relate primarily to limitations regarding what materials may be characterized, the latter issue relates to the degree to which a material may be characterized.

Regarding the latter, in an effort to assess the viability of PLM as a characterization method for CPFEM simulations, it is of interest to determine the consequences of PLM orientation ambiguity on CPFEM deformation predictions. In this study, we attempt to quantify the statistical variability in the differences of the predicted stress fields between a reference sample and a suite of altered samples with random rotations about each crystal's c axis (mimicking random guesses to the full orientation as if they were unknown from PLM measurement). We focus particularly on stress owing to its importance in yield, failure, and fatigue criteria. We analyze the datasets in an effort to determine how the differences in stress fields evolve as a function of the macroscopic strain state, from elasticity, through the elastic–plastic transition, to fully-developed plasticity.

Section 2 details the background and modeling methodology utilized in this study, Section 3 details construction of virtual polycrystalline samples and the simulation suite performed in this study, Section 4 details the analysis used to compare simulations and primary results, Section 5 gives an in-depth look into the results and trends, and Section 6 gives concluding remarks regarding PLM and its consequences with regard to deformation modeling.

## 2. Background and methods

# 2.1. Polarized light microscopy

Large-area grain orientation mapping using PLM is growing in popularity, especially for titanium alloys, due to the ease of sample preparation combined with the ability to map large areas at a fraction of the time compared to other techniques such as EBSD [27]. Current automated PLM systems provide a scan resolution below 1 µm, which is coarser than electron microscope based methods but adequate for many materials science and engineering applications-i.e., it is of sufficient resolution to elucidate the geometric morphology of the microstructure (grain sizes and shapes). However, the relatively fast data collection rate of 150,000 pixels/second enables larger-area PLM measurements in a shorter amount of time compared to EBSD [28]. Consequently, this facilitates the ability to characterize larger areas of material, more points of material within a component, or a wider array of samples/materials as compared to EBSD. Further, PLM relies on relatively simple equipment compared to EBSD, reducing overall system cost [25,26].

For demonstration, Fig. 1 depicts a PLM grain c axis orientation map measured from a 25.4 mm diameter Ti–7Al sample using the TiPolar-S microscope manufactured by MRL Materials Resources, LLC. The system offers interchangeable objective lenses and a 2D translation stage, enabling measurement of samples with dimensions of up to approximately 100 mm  $\times$  125 mm. Though not as stringent, surface polishing requirements sufficient for EBSD also suffice for PLM measurement. The sample presented in Fig. 1 was prepared by polishing

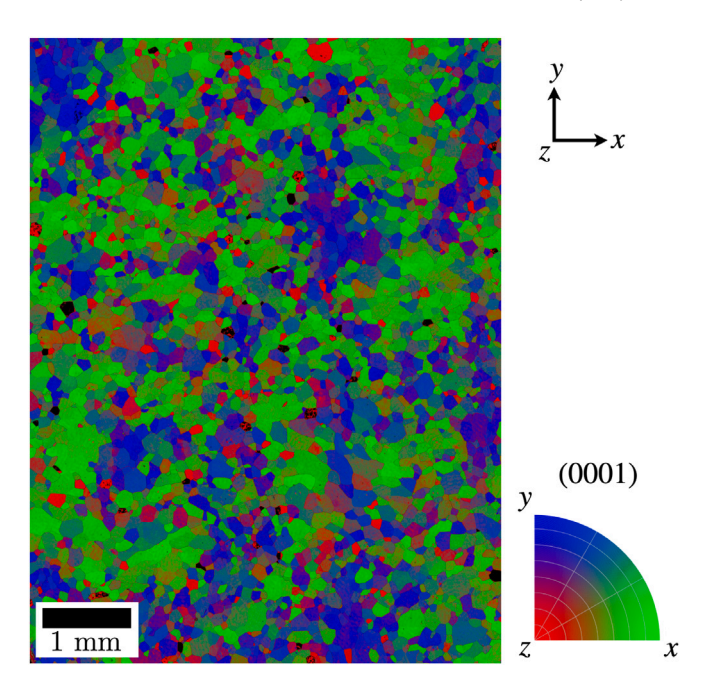


Fig. 1. Example PLM image of a Ti–7Al sample with dimensions of approximately  $5.3 \text{ mm} \times 7.0 \text{ mm}$ , shown with color scale depicting the orientation of the crystal (0001) direction with respect to the sample axes. (For interpretation of the references to color in this figure legend, the reader is referred to the web version of this article.)

the surface using silicon carbide grinding papers (240 grit through 600 grit) followed by vibratory polishing on  $50\,\mathrm{nm}$  colloidal silica. Measurements were conducted using a  $20\times$  objective lens with  $4\times4$  pixel binning. This microscope configuration provides a  $0.792\,\mu\mathrm{m}$  effective pixel size after binning. Automated sample measurement spanned about 5 h for the region presented. We note that binning does not increase measurement speed, but rather reduces the size of the resulting data. The interchangeable objective lens can be paired with the desired pixel binning size to achieve the desired final resolution.

The primary limitation with PLM, however, is its inability to measure the full crystallographic orientation of grains. For HCP materials, PLM can determine the orientation of the c axis, but not the rotation about the c axis. The orientation of the crystal is thus left partially ambiguous. The consequence of this orientation ambiguity is perhaps best understood by inspecting the Euler-Bunge parameterization [29]. Euler-Bunge angles follow a z-x-z convention—i.e., a rotation about the z axis of the crystal (angle  $\phi_1$ ), followed by a rotation about the x axis of the crystal (angle  $\phi_1$ ), finally followed by a second rotation about z axis of the crystal (angle  $\phi_2$ ) performed in succession. The utility of this parameterization is that (for HCP crystals) the first two rotations determine the orientation of the crystal's c axis, while the third angle describes the rotation about the crystal's c axis. In other words, in the Euler-Bunge convention, PLM is able to determine  $\phi_1$  and  $\phi$ , while  $\phi_2$  is left unknown.

We may also demonstrate the effects of PLM's orientation ambiguity by inspecting the bulk collection of orientations, or crystallographic texture. When measuring orientations via PLM, we are left with the full determination of only the  $(0\,0\,0\,1)$  pole figure (PF). In other words, we have access to the information of only one crystallographic fiber, which is insufficient to construct a deterministic orientation distribution function (ODF) for generalized crystallographic textures. To visualize this, we present an example case beginning with a known ODF, plotted in the hexagonal fundamental region of Rodrigues space shown in Fig. 2(a). For demonstration, we choose a simple point texture at the origin of Rodrigues space (a "basal" texture). We plot the corresponding  $(0\,0\,0\,1)$  PF for this ODF in Fig. 2(b). Upon inverting this PF to an ODF  $[3\,0]$  – the result depicted in Fig. 2(c) – we are unable to invert

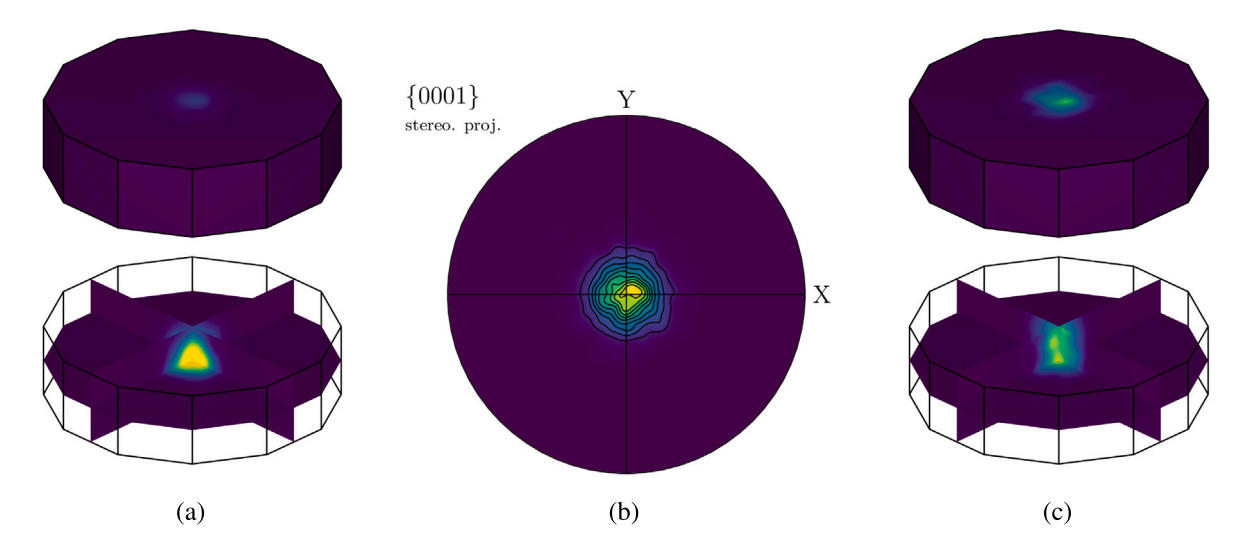


Fig. 2. (a) Example orientation distribution function (ODF) plotted on in the hexagonal fundamental region of Rodrigues space showing the surface and select interior slices of the fundamental region for a basal-type texture (i.e., a point texture centered at the origin of the fundamental region), (b) the corresponding (0001) pole figure (PF) derived from the known ODF plotted as a 2D stereographic projection, and (c) the ODF inverted from only the (0001) PF, depicting a fiber texture. Scale bars are omitted in an effort to highlight the character of the texture distributions rather than absolute magnitudes.

the correct initial ODF, as we have insufficient information regarding the full orientations of the crystals. While the known ODF depicts a point texture, the ODF as found by inverting the (0001) depicts a fiber texture (see: Appendix A, Figure 11 of [31] for a depiction of select HCP fibers in Rodrigues space).

Overall, it is envisioned that PLM can be utilized in a CPFEM workflow primarily to inform the generation of virtual samples in a similar way as EBSD characterization data. In essence, grain maps (revealing grain size, shape, and spatial distribution) can be utilized to inform the geometric morphology of the virtual microstructure, and measured orientations can inform the selection of virtual orientations. Specifically regarding morphology, various studies have demonstrated the established EBSD-to-CPFEM pipeline utilizing 2D surface scans to inform 3D virtual sample generation, using either statistical [32,33] or qualitative means [34]. Various other methods such as Schwartz-Saltykov [35], oblique-sections [36], and the Markov approach [37] aid in extension of 2D data to 3D samples. Regarding orientations, EBSD data may be utilized to generate an ODF from which orientations may be sampled [38,39], or measured orientations can be directly utilized [40]. We assert that PLM can be used in a similar manner as demonstrated for EBSD, with the caveat that orientations will not be fully known (as described previously)—the consequence of which is unknown and necessitates this study.

## 2.2. Crystal plasticity finite element method

To perform CPFEM simulations, we utilize the open source software package FEPX (Finite Element Polycrystal Plasticity) [41,42]. FEPX is a non-linear finite element solver capable of considering both the anisotropic elastic and plastic deformation responses of high-fidelity polycrystalline samples. FEPX considers ductile, quasi-static deformation and isothermal conditions, and is parallelized via OpenMPI to facilitate large simulations. Generally, virtual polycrystalline samples consist of  $\mathcal{O}(100)$  to  $\mathcal{O}(1000)$  of discrete grains, each discretized into  $\mathcal{O}(100)$  to  $\mathcal{O}(1000)$  of elements (both the polycrystal and the attendant finite element mesh are generated via Neper [43], whose capabilities and uses are summarized later in Section 3.1). Here, we briefly describe the basics of the kinematics and models employed in FEPX, and refer the reader to [41] for an in-depth discussion of the kinematics, models, and finite element implementation.

First, FEPX considers a multiplicative decomposition of the deformation gradient at each material point:

$$\mathbf{F} = \mathbf{V}^e \mathbf{R}^* \mathbf{F}^P, \tag{1}$$

where the total deformation gradient,  $\mathbf{F}$ , is decomposed into an elastic stretch (specifically the left elastic stretch tensor),  $\mathbf{V}^e$ , a rotation,  $\mathbf{R}^*$ , and a portion governed by the plastic response,  $\mathbf{F}^P$ .

Focusing first on elasticity, we assume that the elastic strains  $e^e$  present in the body are small: an apt assumption for metallic materials where the critical resolved shear stress is considerably less than the elastic moduli. As such, the left elastic stretch tensor may be approximated as:

$$\mathbf{V}^e = \mathbf{I} + \boldsymbol{\epsilon}^e. \tag{2}$$

The stress is related to the strain via the constitutive relationship (Hooke's law):

$$\tau = \mathbf{C}\epsilon^e$$
, (3)

where  $\tau$  is the Kirchhoff stress and C is the anisotropic stiffness matrix, which is orientation dependent and is reduced due to the symmetry of the crystal [44].

Focusing on plasticity, we employ a rate-dependent restricted-slip power law [45] relationship for slip kinetics:

$$\dot{\gamma}^k = \dot{\gamma}_0 \left( \frac{|\tau^k|}{\tau_c^k} \right)^{\frac{1}{m}} \operatorname{sgn}(\tau^k), \tag{4}$$

where  $\dot{\gamma}^k$  is the shear rate on the kth slip system,  $\dot{\gamma}_0$  is a scaling coefficient,  $\tau$  is the resolved shear stress,  $\tau_c$  is the critical resolved shear stress, and m is the rate dependence parameter.

We evolve the critical resolved shear stress of each slip system via a saturation model:

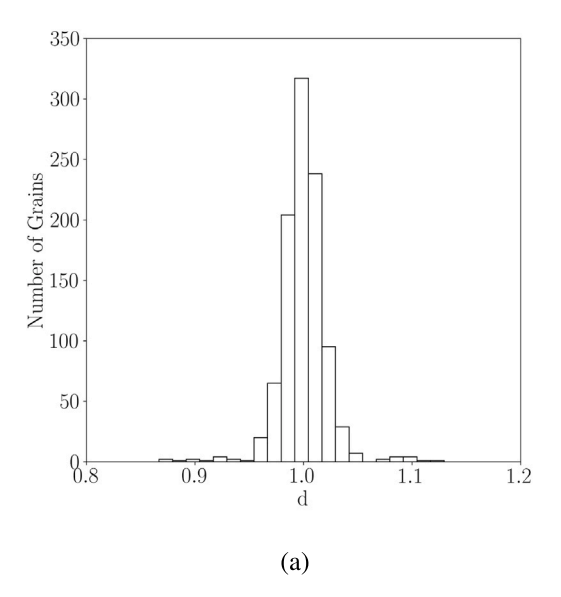
$$\dot{\tau}_c^k = h_0 \left( \frac{\tau_s^k (\dot{\gamma}) - \tau_c^k}{\tau_s^k (\dot{\gamma}) - \tau_0^k} \right) \dot{\Gamma},\tag{5}$$

where  $h_0$  is a scaling coefficient,  $\tau_s$  is the saturation critical resolved shear stress, and  $\dot{\Gamma}$  is the sum of the absolute value of all shearing rates at the material point (i.e., sum over k). We assume isotropic hardening, where all slip systems harden such that (for HCP crystals) the ratios of the initial strengths remain constant throughout deformation. This ensures that the single crystal yield surface retains its shape in deviatoric stress space throughout plastic deformation.

We evolve the orientation of the crystal lattice (here parameterized via the Rodrigues vector,  $\mathbf{r}$ ) via:

$$\dot{\mathbf{r}} = \frac{1}{2} \left( \boldsymbol{\omega} + \left( \boldsymbol{\omega} \cdot \mathbf{r} \right) \mathbf{r} + \boldsymbol{\omega} \times \mathbf{r} \right), \tag{6}$$

where  $\omega$  is the lattice spin vector (itself ultimately dependent on both  $\dot{\gamma}^k$  and  $\mathbf{R}^*$ , described in full in [41]).



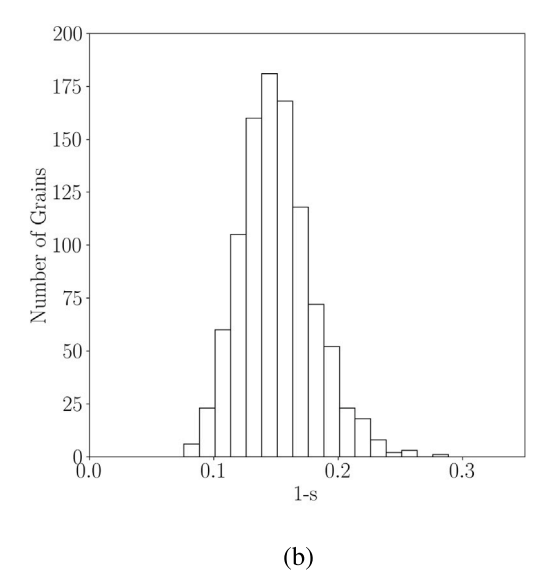
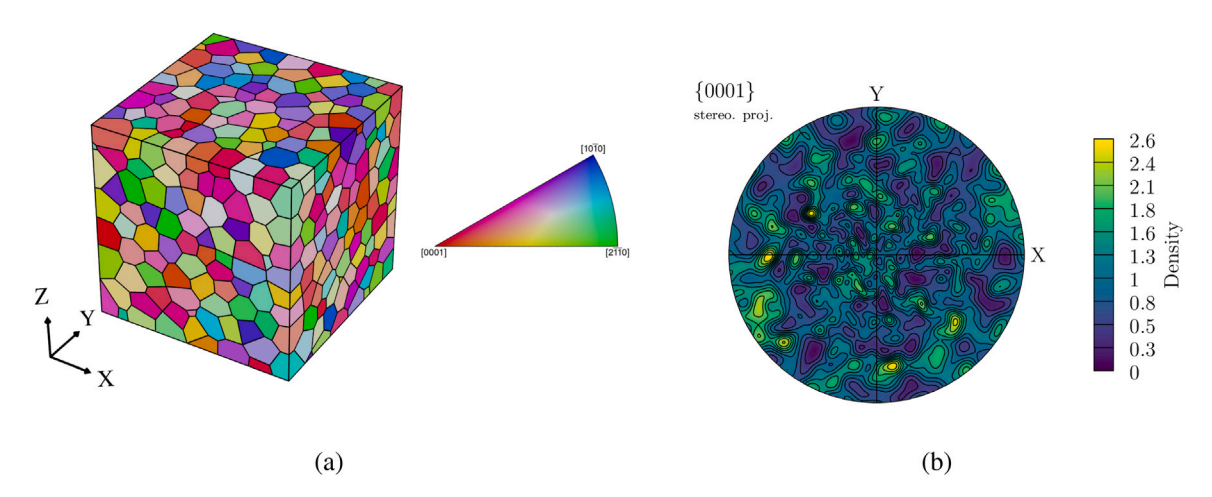


Fig. 3. (a) Grain size distribution, depicted as a histogram of the value d, the normalized equivalent grain diameter and (b) grain shape distribution, depicted as a histogram of the value 1 - s, where s is the sphericity.



**Fig. 4.** (a) Virtual polycrystalline sample generated via Neper, depicting a highly-equiaxed grain morphology, and a random orientation distribution (colored via the standard IPF color map for HCP crystals with respect to the sample z axis) and (b) corresponding (0001) pole figure. This pole figure is identical for all simulations in the primary simulation suite, owing to the similar c axis fields for each sample. (For interpretation of the references to color in this figure legend, the reader is referred to the web version of this article.)

## 3. Simulations

In this section, we describe the generation of simulations to probe the effects of orientation ambiguity on CPFEM deformation predictions. We construct a suite of simulations, consisting of a reference simulation and ten simulations in which each crystal is rotated by its c axis by a random amount. The sample morphology is fixed from sample-to-sample to isolate the effects of the rotation about the crystals' c axes, and an idealized sample is generated from hypothesized morphological statistics (mimicking what could be gathered from experimental data). Ultimately, the differences in predictions from simulation-to-simulation compared to the reference allows for quantification of the consequence of orientation ambiguity.

We are careful to note here the limitations of the present study. In an effort to provide crucial first insight on the consequences of PLM orientation ambiguity on CPFEM predictions, we limit the scope of the simulation parameter space that we explore. Namely, we consider only a single material, an equiaxed microstructure with randomly generated crystallographic orientations. Further, we consider only uniaxial deformation to a state before the ductility limit of the sample. While we anticipate that these simulation parameters (i.e., material system,

crystallographic texture, deformation history) could influence results, understanding this behavior is best reserved for future studies with more focus on these individual aspects.

## 3.1. Polycrystal and mesh generation

Here, we generate a virtual polycrystalline sample and its attendant finite element mesh via Neper [42,43], which is capable of enacting statistical control of grain size and grain shape distributions as dictated by user input. To gather a large amount of statistics per sample, we choose to create a sample with 1000 grains. We opt for a sample containing relatively equiaxed grains in an attempt to reduce microstructural effects. This morphology is achieved by targeting a Dirac distribution with a mean value of 1 for the normalized equivalent diameter, d (i.e., grain size), and by targeting a lognormal distribution with a mean of 0.145 and a standard deviation of 0.03 for the sphericity, s (or more specifically a distribution of 1 - s). We choose a domain to be a cube with side length 1 mm (note that the crystal plasticity model described in the preceding section contains no inherent length scale, and we provide units herein for a sense of consistency). Statistics concerning the distributions of grain size and shape for the polycrystal are depicted

**Table 1** Single crystal elastic constants for the  $\alpha$  phase of Ti–6Al–4V [32].

	1		
C <sub>11</sub> (GPa)	$C_{12}$ (GPa)	C <sub>13</sub> (GPa)	$C_{44}$ (GPa)
169.7	88.7	61.7	42.5

**Table 2** Plasticity modeling parameters for the  $\alpha$  phase of Ti–6Al–4V [32].

$\tau_{0,b}$ (MPa)	$\tau_{0,p}$ (MPa)	$\tau_{0,\pi}$ (MPa)	m	$\dot{\gamma_0}$ (s <sup>-1</sup> )	$h_0$ (MPa)	$\tau_s$ (MPa)
390	468	663	0.01	1	190	530

in Fig. 3. We further plot the resulting virtual polycrystal sample in Fig. 4(a).

#### 3.2. Orientation generation

Generally, orientations in FEPX are considered on a per-element basis (i.e., in the presence of initial intragranular misorientation) or on a per-grain basis (i.e., each element in the grain is assigned the same orientation, assuming each grain is a single crystal). Here, we opt for the latter paradigm to simplify the influences at play. We again utilize Neper to generate and assign the orientations. In this first effort, we assume a random orientation distribution function applied randomly to all grains in an effort to span the fundamental region of Rodrigues space (i.e., probe a wide range of orientations) and to randomize neighborhood effects (i.e., no preferential neighboring orientations, or microtexture). The resulting distribution of orientations is depicted as an (0001) pole figure in Fig. 4(b). Furthermore, we visualize the orientations on the finite element mesh of the virtual microstructure using the standard IPF color map, depicted in Fig. 4(a).

#### 3.3. Modeling parameters

We choose the  $\alpha$  phase of Ti–6Al–4V owing to its HCP crystal structure, the extensive attention it has been given in literature and the resulting high degree of confidence in its elastic/plastic behavior and modeling parameters [32,34,46], and its applicability as a surrogate for the class of Ti–Al alloys. Additionally, Ti–6Al–4V possesses a moderate degree of elastic and plastic anisotropy. The crystal plasticity parameters for the  $\alpha$  phase of Ti–6Al–4V are shown in Tables 1 and 2, where Table 1 lists elastic constants of the  $\alpha$  phase of Ti–6Al–4V, while Table 2 lists the plastic modeling parameters [47].

# 3.4. Boundary conditions and deformation history

We choose to employ so-called "minimal" boundary conditions to apply uniaxial tensile deformation with minimally invasive constraints (i.e., an attempt to minimize the number of fixed nodes while disallowing unconstrained rigid body motion and rotation, see: [48]). To apply deformation, we fix all nodes on one face in the tensile direction, while applying a non-zero velocity to all nodes of the opposing face (we refer to these two faces collectively as the "control surfaces"). The other surfaces were left traction free. The boundary conditions are displayed in a simplified schematic in Fig. 5. Here, we choose the z axis as the tensile axis.

Regarding the deformation history, we impose a constant strain rate of  $1\times 10^{-3}~{\rm s}^{-1}$  (i.e., fully within the quasi-static regime) in an attempt to mitigate large rate dependency effects on the deformation response. Velocities are calculated internally in FEPX to satisfy the applied strain rate. FEPX applies a load history in discrete steps. We apply these steps to a sufficient maximum strain and at a sufficient resolution to allow for consideration of the deformation response at various representative points of the deformation history. In particular, we will present data at macroscopic strain states of 0.4% (in the macroscopic elastic regime),

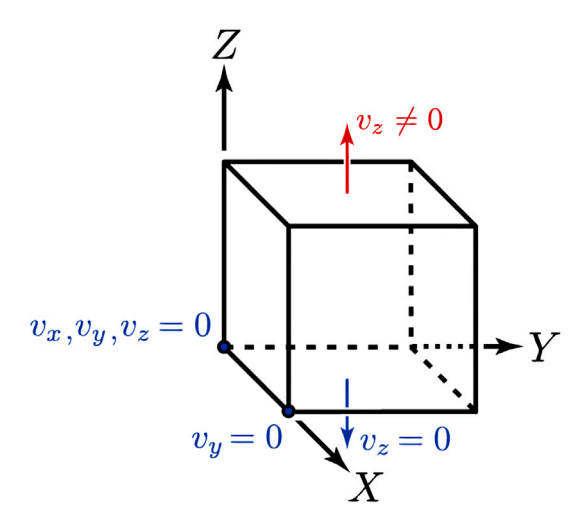


**Fig. 5.** A schematic depicting the minimal boundary conditions as applied to the polycrystal in this study. The loading direction is in the sample "z" direction, and the velocities on the "z" surfaces are applied to all nodes on those surfaces. The two nodes with additional boundary conditions pin the sample to prevent rigid body translation and rotation. Figure reproduced from the FEPX documentation [48].

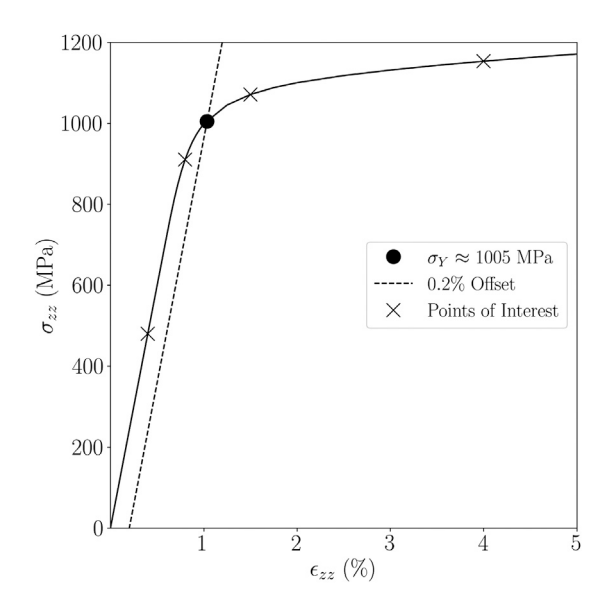
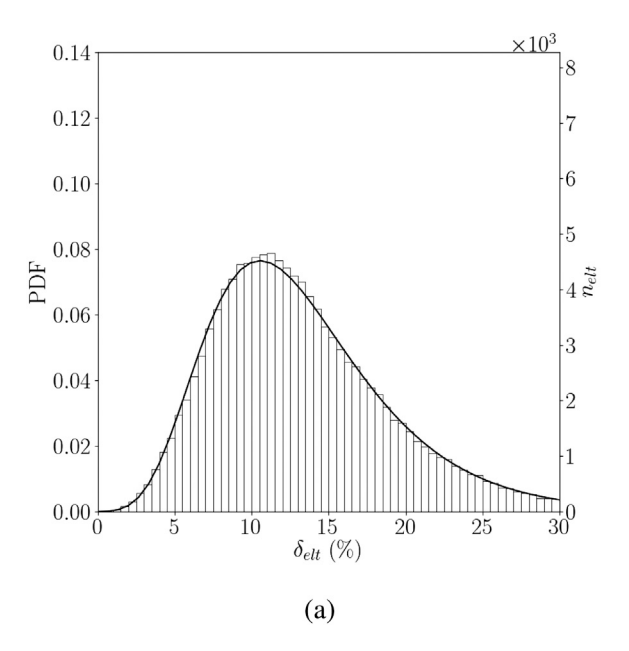


**Fig. 6.** Stress–strain curve of the reference simulation, depicting the overall mechanical behavior of the polycrystal. The 0.2% offset yield point is depicted, along with the four macroscopic states of interest at 0.4%, 0.8%, 1.5%, and 4.0% strain—i.e., two points nominally in the elastic regime, and two points nominally in the plastic regime.

0.8% (shortly before macroscopic yield), 1.5% (shortly after the elastic-plastic transition), and 4% (near the ductility limit). A representative macroscopic stress–strain curve (of the reference simulation described below in Section 3.5) is shown in Fig. 6, with the macroscopic states of interest marked along the deformation history.

## 3.5. Simulation suite

To determine the effect that orientation ambiguity has on the deformation response as predicted via CPFEM, we perform a suite of simulations where the crystallographic orientations are purposefully altered from a reference sample. In total, we generate one reference sample, and ten altered samples. In the ten altered samples, all aspects are held fixed compared to the reference sample except for the crystallographic orientations.



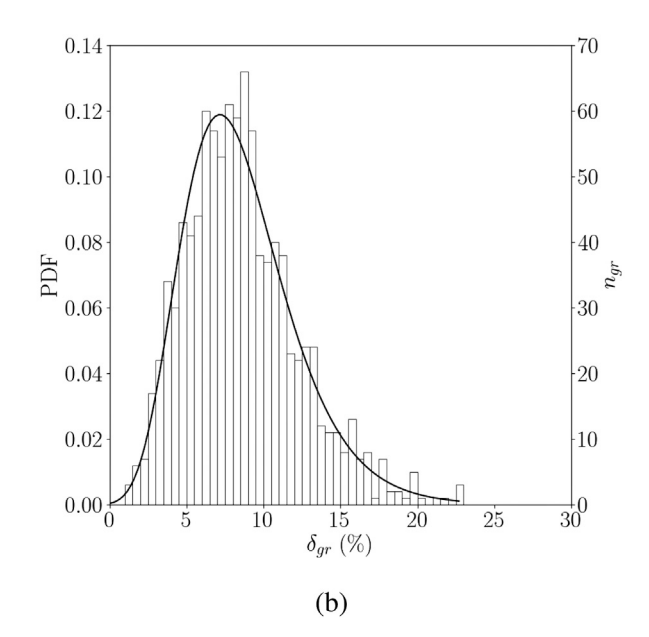


Fig. 7. Distributions of stress differences between a single altered simulation and the reference simulation at 1.5% macroscopic strain at (a) the element scale, and (b) the grain scale. Lognormal fits to the data (solid lines, scale on left vertical axes) are overlayed atop the raw data (histograms, scale on right vertical axes).

We generate the orientations in the ten altered samples directly from the orientations of the reference sample. The Euler-Bunge convention is chosen for parameterization, such that we have univariate control over the rotation about each crystal's c axis via alteration of the third Euler-Bunge angle,  $\phi_2$  (see Section 2.1). In each altered sample, we randomly change each grain's orientation separately by rotating  $\phi_2$  by a random amount within  $\Delta \phi_2 = \pm 30^\circ$ , the range of which we choose to constrain the rotation of each crystal within a local fundamental zone (i.e., any rotation outside of this range is a symmetric equivalent to a rotation within the range). Overall, each sample is thus c-axis-similar: i.e., the caxis field across the domain of each sample is identical, but the rotation about the c axis for each crystal in each sample is different. As such, all simulations will have an identical (0001) pole figure (depicted in Fig. 4(b)). Each sample is meant to mimic a random assignment of the third Euler-Bunge angle as if it was unknown (here within the bounds of fundamentally similar orientations from the reference simulation for sake of simplification of analysis).

We hypothesize that differences between the predictions of the reference simulation and those of the altered simulations during the early stages of deformation (i.e., in the presence of low plasticity), will be low owing to the transversely isotropic nature of elasticity in HCP crystals [44,49,50]. However, as plasticity becomes more prevalent, we hypothesize that predictions in stress fields may become more variable (with respect to the reference) as plasticity evolves and deformation proceeds with granular reorientation trajectories that deviate further from the reference. In other words, the path-dependent nature of plasticity at the local scale may lead to stress predictions which deviate more considerably from the reference than in the nominally elastic regime.

#### 4. Results

To begin, we define a metric to quantify the difference in stress predictions for a randomly altered sample against a reference sample:

$$\delta = \frac{\|\Delta\sigma\|}{\|\tilde{\sigma}\|} \cdot 100,\tag{7}$$

a percentage, where  $\tilde{\sigma}$  is the Cauchy stress tensor for the reference sample, and  $\Delta \sigma$  is the difference between the reference sample stress tensor and the stress tensor for an altered sample, or:

$$\Delta \sigma = \tilde{\sigma} - \sigma. \tag{8}$$

The magnitude of the stress tensors is generally calculated as a scaling of the tensor inner product, or:

$$\|\sigma\| = \sqrt{\frac{3}{2}\sigma : \sigma},\tag{9}$$

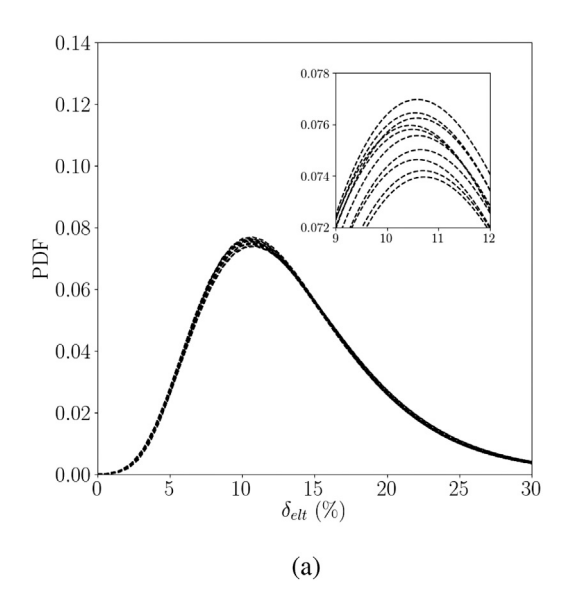
and is utilized for both the difference tensor and the reference stress tensor in Eq. (7).

This difference metric may be applied at various scales. For the study at hand, we choose to calculate  $\delta$  at the element scale ( $\delta_{elt}$ ), the grain scale ( $\delta_{gr}$ ), and the domain scale ( $\delta_{dom}$ ), by utilizing the elemental stresses, the volume-weighted grain-averaged stresses, and the volume-weighted domain-averaged stresses, respectively. Volume weighted averages are calculated as:

$$\bar{\sigma} = \sum_{i=1}^{n_{elt}} \frac{V_i}{V_{tot}} \sigma_i, \tag{10}$$

where  $\bar{\sigma}$  is a volume-averaged stress quantity (which may be used directly in Eqs. (7)–(9)),  $n_{elt}$  refers to the number of elements per grain or the number of elements in the domain and  $V_{tot}$  refers to either a grain volume or the domain volume, when calculating grain-averaged stresses or domain-averaged stresses, respectively. The calculation of the differences at various scales facilitates insight into the effect of c axis ambiguity at various scales, where certain predictions or comparisons may take place. For example, certain fatigue models may be influenced by local behavior and would be more susceptible to variability at the element scale, while comparisons to high-energy X-ray diffraction experiments will take place at the grain scale.

To motivate a reduction in amount of data to be presented in coming sections, we first present a histogram containing distributions of  $\delta_{elt}$  and  $\delta_{gr}$  (Figs. 7(a) and (b), respectively) at a macroscopic strain of 1.5%. The lognormal distribution fit is overlayed on each plot, and we note that it corresponds to the raw histograms to a generally acceptable degree. Consequently, for sake of clarity in the presentation of data herein, we choose to depict probability density functions using lognormal distributions rather than the raw histograms. Further, as shown in Fig. 8 which depicts the lognormal distributions of  $\delta_{elt}$  and  $\delta_{gr}$  for all 10 altered simulations at a macroscopic strain of 1.5%, we note that the results from simulation-to-simulation show little appreciable difference. Since the statistical results for each sample are similar, we conclude that each individual sample is representative of the population. Consequently, we will present data from only a single altered sample



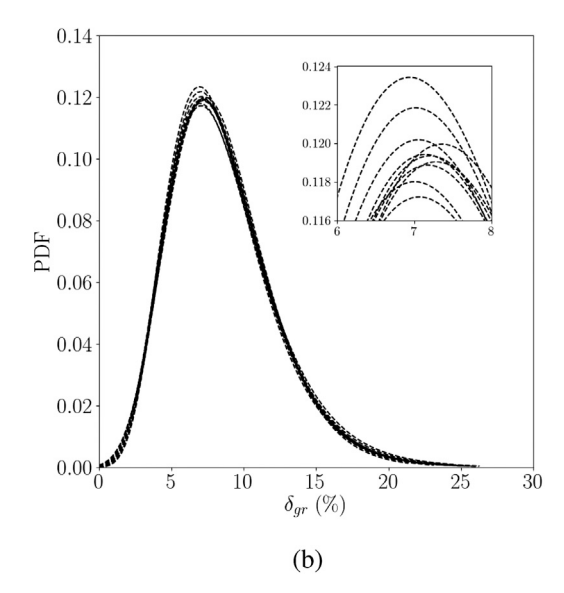


Fig. 8. Lognormal distribution fits of stress differences between all ten altered simulations and the reference simulation at 1.5% macroscopic strain at (a) the element scale, and (b) the grain scale. Insets in each plot offer detail near the distribution peaks.

Table 3

Domain scale stress differences at the four macroscopic strain states of interest.

€ (%)	$\delta_{dom}$ (%)
0.4	0.001
0.8	0.002
1.5	0.166
4.0	0.185

compared to the reference sample for sake of clarity and brevity. This is further exemplified through inspection of the macroscopic behavior of the samples, specifically the elastic modulus (120.44  $\pm$  0.037 GPa), yield stress at 0.2% offset strain (1005.58  $\pm$  1.41 MPa) and stress at 5% strain (1168.82  $\pm$  2.35 MPa), where the low standard deviations indicate nearly identical macroscopic behavior in all 11 samples.

In sum, Fig. 9 depicts the lognormal distributions of  $\delta_{elt}$  and  $\delta_{gr}$  at the macroscopic strain states of interest (see: Section 3.4) considering every element in the domain of the sample. Additionally, since the error calculations in Eqs. (7) through (9) result in a single scalar value, the results for  $\delta_{dom}$  are presented not in a figure, but Table 3.

## 5. Discussion

## 5.1. Sample-to-sample differences

As initially discussed in Section 4, we observe that the differences from sample-to-sample is low. The data presented in Fig. 8 (for sake of brevity and clarity, we plot the data from multiple simulations at only one macroscopic state) indicate that there is little difference in the statistical distributions for each altered sample (as showcased at a single macroscopic strain state for sake of clarity). We determine that each sample is statistically representative of the population. Recall that each sample has a random rotation,  $\Delta\phi_2$ , about each crystal's c axis, as altered from the reference simulation. These results do not necessarily indicate that different rotations result in the same local differences, but simply that the distribution of differences is statistically similar. This lends confidence to the choice of 1000 grains in the domain of the polycrystal, which is sufficient in providing stable statistics from sample-to-sample for the microstructure chosen in this study.

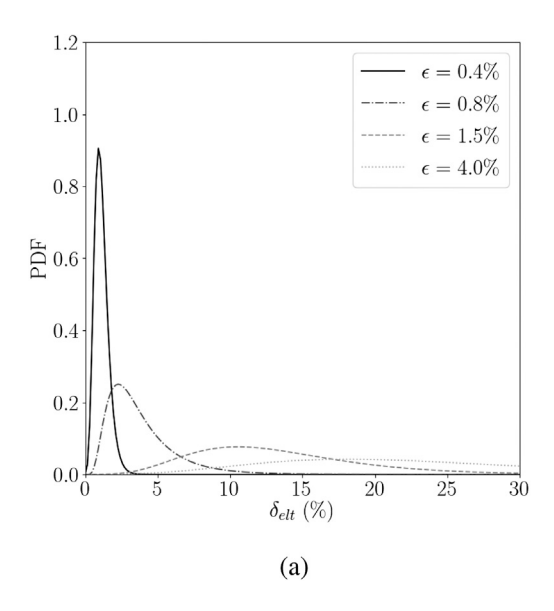
#### 5.2. Element scale differences

We next inspect the distributions of differences in the stress states on an element-by-element basis. Fig. 9(a) depicts the distributions of stress differences at the element scale for the four strain states of interest as depicted in Fig. 6. We first note the general trends with regard to the distributions. Namely, in the elastic regime, the mean differences are generally low, with mean values of 1.13% and 3.82% at 0.4% and 0.8% macroscopic strain, respectively. As we enter the plastic regime, the mean differences begin to increase more dramatically, with mean values of 13.43% and 23.23% at 1.5% and 4.0% macroscopic strain, respectively. We further observe that as the macroscopic strain increases, so too does the spread in the distributions. At low strain states in the elastic regime, the distributions are relatively tight, with standard deviations of 0.48% and 2.31% at 0.4% and 0.8% macroscopic strain, respectively. In the plastic regime, we observe much broader distributions, with standard deviations of 6.15% and 11.01% at 1.5% and 4.0% macroscopic strain, respectively. Overall, we interpret the lower differences in the elastic regime as a function of the transversely isotropic nature of hexagonal crystals. As the amount of plasticity increases across the domain of the sample, so too does the difference in stresses owing to the potential for different slip systems to activate as a function of orientation difference from reference.

## 5.3. Grain scale differences

Considering volume-weighted grain-averaged stresses (see Eq. (10)), we observe similar trends as those observed in the element scale analysis. Fig. 9(b) depicts the distributions of stress differences at the grain scale for the four strain states of interest. We again observe that as the macroscopic strain increases, so too does the mean in the stress differences, with mean values 0.87%, 2.77%, 8.58%, and 12.29% at 0.4%, 0.8%, 1.5%, and 4.0% macroscopic strain, respectively. Further, as we increase the macroscopic strain, the spread in the difference distributions also increase, with standard deviations of 0.39%, 1.71%, 3.66%, and 5.18% at 0.4%, 0.8%, 1.5%, and 4.0% macroscopic strain, respectively. Considering these values, we again note that there is a large increase in stress differences at or shortly after the elastic–plastic transition.

Comparing to the element scale analysis, we find that overall both the means and the standard deviations of the distributions are considerably lower in all cases at the grain scale. Our interpretation of this



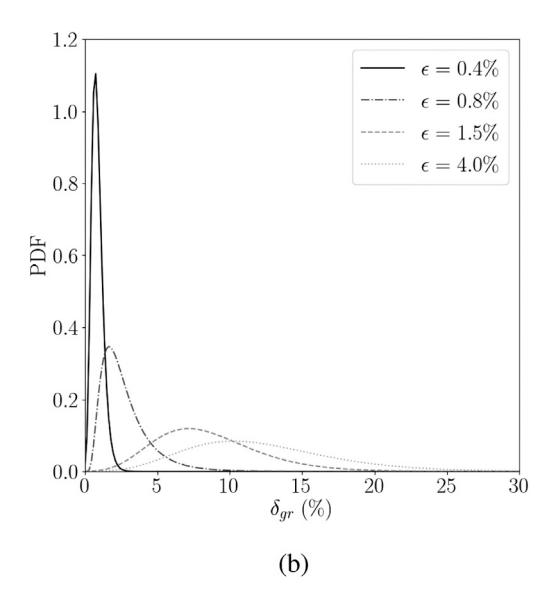
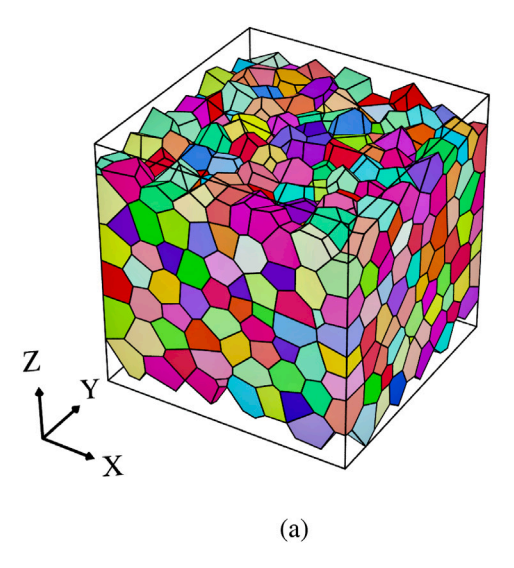


Fig. 9. Lognormal distribution fits of stress differences between the first altered simulation and the reference simulation for the four macroscopic strain states of interest at (a) the element scale, and (b) the grain scale.



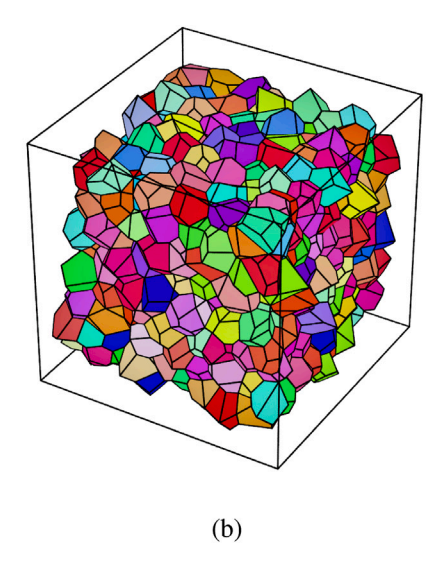


Fig. 10. Depictions of the datasets utilized in the analyses considering (a) removal of grains abutting the control surface, and (b) removal of grains along all domain surfaces. Grains are colored identically to those in Fig. 4(a), utilizing the inverse pole figure colormap in that image. (For interpretation of the references to color in this figure legend, the reader is referred to the web version of this article.)

trend is that each grain, thus, has a heterogeneous distribution of stress differences at the element scale, which is obscured when averaged at the grain scale. In other words, outlier values will be averaged-out, and the resulting distributions at the grain scale will overall shift downward in terms of differences.

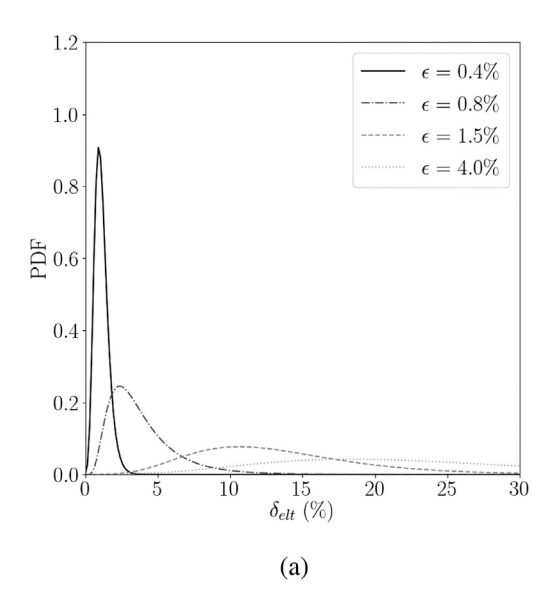
# 5.4. Domain scale differences

Considering volume-weighted domain-averaged stress, we observe somewhat similar trends as in both the element scale analysis and the grain scale analysis. The calculated differences in the domain-averaged stress between the altered simulation and the reference simulation at the four strain states of interest are presented in Table 3. The differences in the stress state are again lower in the nominally elastic regime than those in the plastic regime. We note that the differences in the stresses are much smaller at the domain scale than at either the element scale or the grain scale. We interpret these values in light of the fact that the texture of the samples are random. Random rotations about the c axis of each crystal will itself result in a random texture. With a

sufficient number of grains within the domain, it should be expected that the overall macroscopic response of the sample will be similar, as demonstrated. This may not be the case for samples displaying nonrandom textures, where random rotations about the c axis of each crystal may have more appreciable impact on the texture of the sample. However, based on the general trend of results when moving "upward" in scales, we still expect that overall the domain scale results will be smaller than those at both the elemental and grain scales.

# 5.5. Investigation of spatial variation

We now probe the data sets to investigate whether there is a correlation between spatial location and a difference in stress prediction in an attempt to narrow down primary influences on behavior. The analysis in this section is focused on the removal of select elements from the data sets to see if the distributions in stress differences exhibit different character (quantitatively and qualitatively) than those when considering all data points within the domain. We consider three different cases: the first where grains on the control surface (and their associated



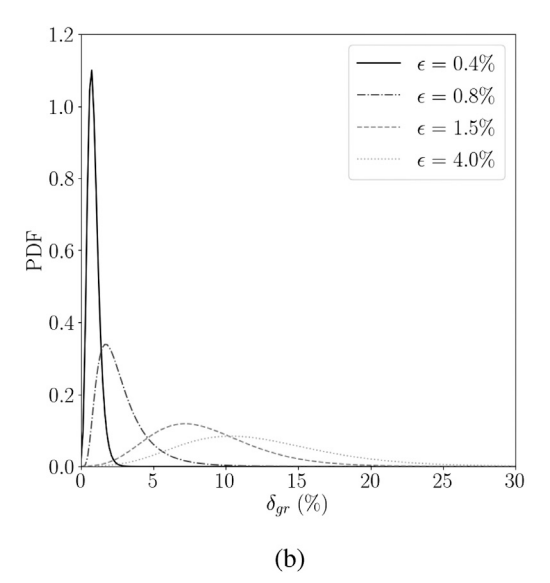
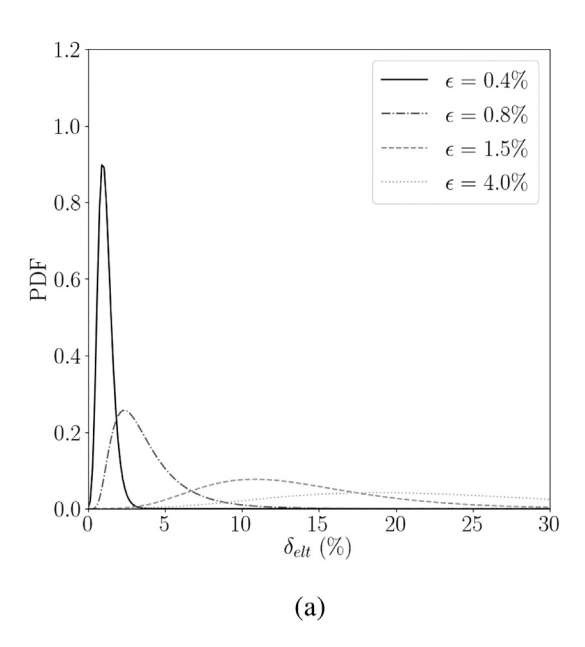


Fig. 11. Lognormal distribution fits of stress differences between the first altered simulation and the reference simulation for the four macroscopic strain states of interest and considering the removal of grains abutting the control surface from analysis at (a) the element scale, and (b) the grain scale.



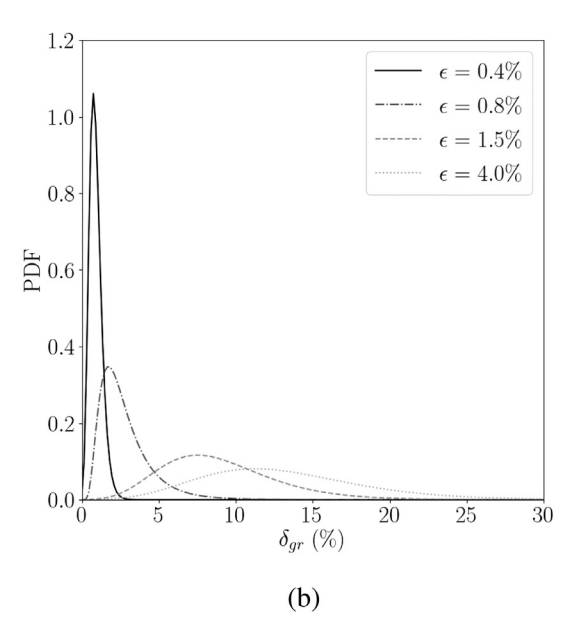


Fig. 12. Lognormal distribution fits of stress differences between the first altered simulation and the reference simulation for the four macroscopic strain states of interest and considering the removal of grains abutting all domain surfaces from analysis at (a) the element scale, and (b) the grain scale.

elements) are removed from the data set for analysis (Section 5.5.1), the second where grains on all surfaces of the domain including traction free surfaces (and their associated elements) are removed from the data set for analysis (Section 5.5.2), and the third where the elements along grain boundaries are removed from the data set for analysis (Section 5.5.3).

## 5.5.1. Removing control surfaces

Here, we repeat the primary statistical analysis, though with a data set reduced by removing grains on the control surface of the sample from consideration in the analysis. Particularly, this analysis will reveal if there are any undue influences due to the boundary conditions on the sample, which will be most acute and evident in the grains which abut the surfaces where the boundary conditions are applied. As we describe in Section 3.4, the axial control surfaces are the sample z surfaces (i.e., the surfaces where  $\pm z$  is the normal). Fig. 10(a) depicts the grains remaining in the domain. We select all remaining

elements for our calculations, and in particular we note that the domain scale results consider only these remaining elements. This provides further justification for the use of probability density functions over histograms, as they may be directly compared against reduced data sets, whereas histograms will necessarily have lower counts owing to the reduction in number of elements or grains making comparisons more difficult.

Distributions of stress differences at the element scale for the remaining elements are depicted in Fig. 11(a), distributions of grain scale stress differences are depicted in Fig. 11(b), and domain scale differences are summarized in Table 4. We again report all results by comparing only the first sample to the reference sample, and at the same four macroscopic strain states of interest. Means of the element scale distributions in Fig. 11(a) are calculated to be 1.13%, 3.90%, 13.46%, and 23.27%, while standard deviations are calculated as 0.48%, 2.34%, 6.08%, and 10.89% at 0.4%, 0.8%, 1.5%, and 4.0% macroscopic strain, respectively. Means of the grain scale distributions

L. van Wees et al.

Domain scale stress differences at the four macroscopic strain states of interest for analysis with grains abutting control surfaces removed from consideration.

€ (%)	$\delta_{dom}$ (%)
0.4	0.003
0.8	0.036
1.5	0.201
4.0	0.218

Table 5

Domain scale stress differences at the four macroscopic strain states of interest for analysis with grains abutting free surfaces removed from consideration.

€ (%)	$\delta_{dom}$ (%)
0.4	0.021
0.8	0.030
1.5	0.378
4.0	0.416

in Fig. 11(b) are calculated to be 0.87%, 2.83%, 8.59%, and 12.30%, while standard deviations are calculated as 0.39%, 1.72%, 3.67%, and 5.15% at 0.4%, 0.8%, 1.5%, and 4.0% macroscopic strain, respectively. We observe that the distributions of stress differences at the elemental and grain scales are seemingly not appreciably altered, with mean values at both the elemental and grain scales roughly corresponding to those gathered in the analysis considering the full domain as presented in Sections 5.2 and 5.3. Likewise, the spreads in the data do not exhibit appreciable difference from those in the full dataset. Finally, while domain scale values show some reduction in differences, it is already at such a relatively small scale that we do not place much significance in these findings, especially considering the results at both the element and the grain scale. Consequently, we interpret these results to mean that the distributions of stress differences within the grains abutting the control surfaces are roughly equivalent to those in the main body of the sample, indicating that boundary conditions have little influence on the observed results.

## 5.5.2. Removing free surfaces

Here, we perform a similar analysis as in the preceding section, but now by reducing the data set by removing grains on the traction free surfaces of the sample from consideration in the analysis, again in an attempt to see if there is any bias of stress differences in these regions. This will specifically exclude grains which abut the x and y surfaces of the sample. Fig. 10(b) depicts the grains remaining in the domain. Again, domain scale results consider only the remaining elements in the data-set.

Overall, we again observe that the distributions of stress differences at the element scale, grain scale, and domain scale all depict similar trends as when considering the entire domain volume. Means of the element scale distributions in Fig. 12(a) are calculated to be 1.15%, 3.83%, 13.67%, and 23.65%, while standard deviations are calculated as 0.48%, 2.22%, 6.08%, and 10.86% at 0.4%, 0.8%, 1.5%, and 4.0% macroscopic strain, respectively. Means of the grain scale distributions in Fig. 12(b) are calculated to be 0.90%, 2.80%, 8.98%, and 13.10%, while standard deviations are calculated as 0.40%, 1.66%, 3.75%, and 5.28% at 0.4%, 0.8%, 1.5%, and 4.0% macroscopic strain, respectively. Domain scale statistics are summarized in Table 5. Overall, this indicates that the grains abutting the free surfaces have roughly the same distributions as the grains within the volume of the domain, as their removal does not alter the character of the distributions of stress differences, indicating that free surfaces have little influence on the observed results.

## 5.5.3. Removing grain boundaries

Here, we repeat the analysis on the data set with elements in the vicinity of grain boundaries removed in an effort to determine

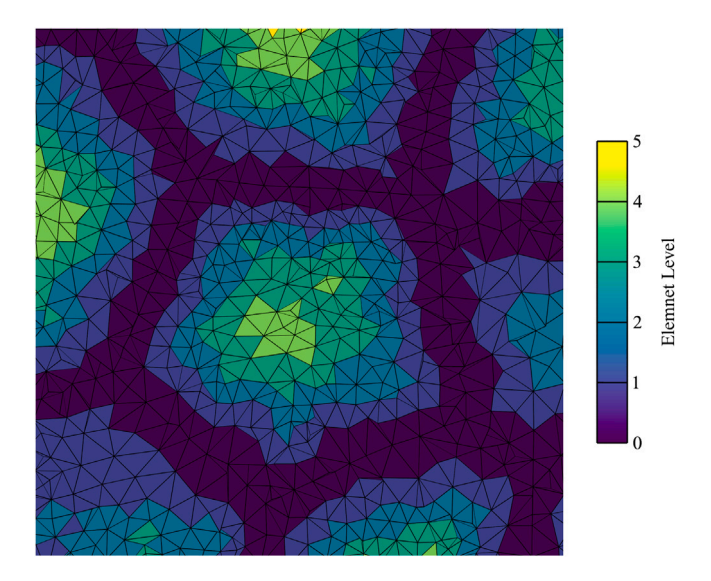
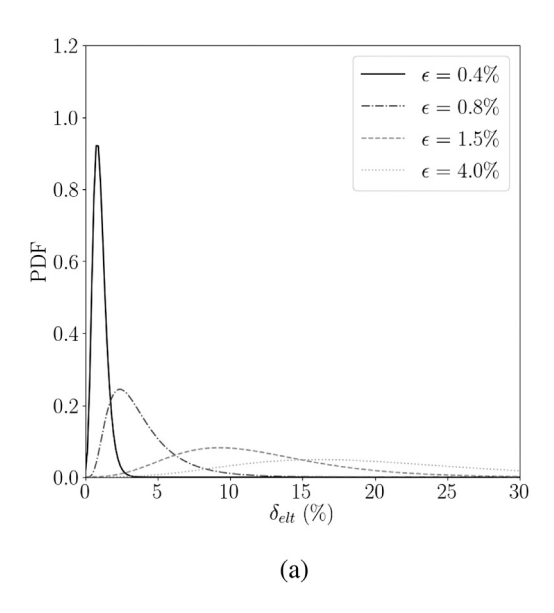


**Fig. 13.** A plot of a slice through the center of the finely-meshed 100 grain polycrystal, depicting the levels at which elements reside relative to the grain boundary, where "level 0" refers to elements that abut a grain boundary, "level 1" refers to elements which abut elements that abut the grain boundary, and so on. (For interpretation of the references to color in this figure legend, the reader is referred to the web version of this article.)

the effects of grain-to-grain interaction. We achieve this by ranking the degree of locality of elements with respect to grain boundaries, which allows us to consider the removal of "level 0" elements (those directly touching the boundary), "level 1" elements (those touching elements which themselves touch the boundary), and so on, akin to peeling layers from an onion. For the 1000 grain polycrystal used in the preceding portions of the paper, we chose a mesh such that there were approximately 100 elements per grain (i.e., approximately 100,000 total elements within the domain). This was meant to facilitate relatively rapid simulations for the 11 simulation test suite. However, for that mesh, we find that the overwhelming majority of elements are "level 0", with only 16 elements greater than "level 0". This does not offer a significant number of elements from which to draw meaningful

Consequently, for this section we generate a new virtual polycrystal. Using the same methods as described in Section 3, we generate a polycrystalline sample with identical parameters (grain size, shape distributions, crystallographic texture) as the 1000 grain sample, but with 100 grains and a finer mesh to provide sufficient resolution for grains containing multiple layers of elements. We plot a slice of the interior of the polycrystal in Fig. 13, where the colors depict the element level (i.e., their relative position with respect to the grain boundary). We note that since we are removing elements from the grains and the domains, both the grain-averaged stresses and the domain-averaged stresses are calculated using only the remaining elements.

Overall, we observe that the distributions of stress variation at the element scale, grain scale, and domain scale do not differ considerably as compared to the entire domain volume. After the removal of the first layer elements, we compute the means of the element scale distributions in Fig. 14(a) as 1.02%, 3.88%, 11.83%, and 20.28%, and the standard deviations as 0.46%, 2.35%, 5.63%, and 9.39% at 0.4%, 0.8%, 1.5%, and 4.0% macroscopic strain, respectively. For the grain scale distributions in Fig. 14(b), we compute the means as 0.88%, 3.00%, 7.78%, and 10.54%, and the standard deviations as 0.43%, 1.74%, 3.38%, and 4.10% at 0.4%, 0.8%, 1.5%, and 4.0% macroscopic strain, respectively. For the removal of the first two layers of elements, we find the means of the element scale distributions to be 0.98%, 3.75%, 11.28%, and 19.32%, and the standard deviations to be 0.44%, 2.22%, 5.13%, and 8.49% at 0.4%, 0.8%, 1.5%, and 4.0% macroscopic



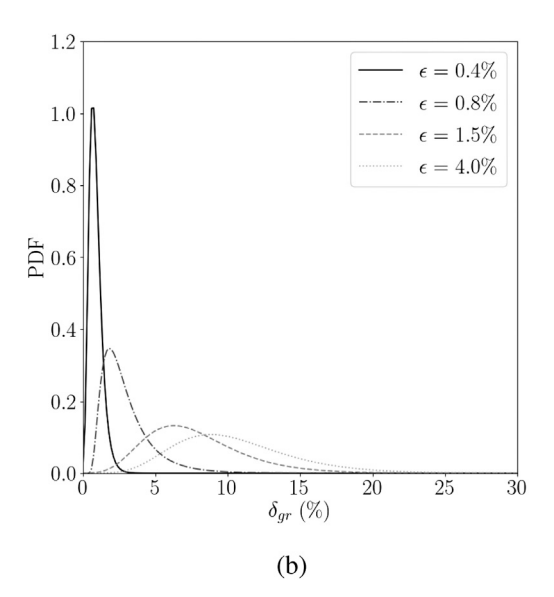
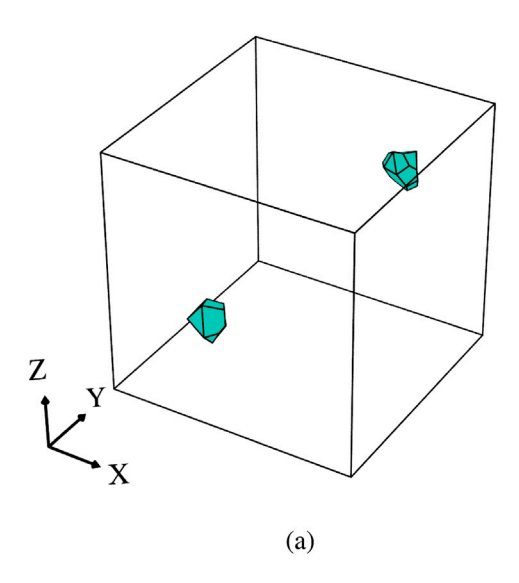


Fig. 14. Lognormal distribution fits of stress differences between the first altered simulation and the reference simulation for the four macroscopic strain states of interest and considering the removal of the first layer of elements abutting the grain boundaries from analysis at (a) the element scale, and (b) the grain scale.



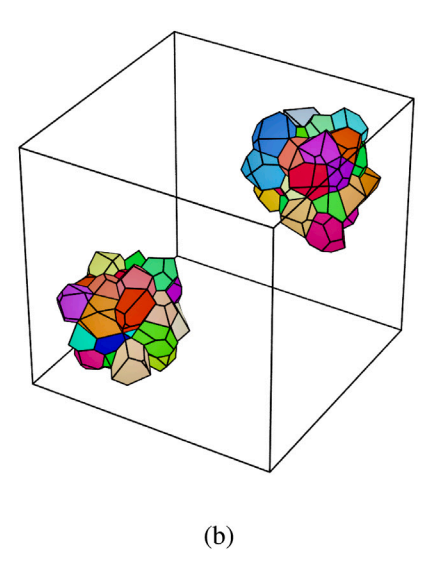


Fig. 15. (a) Two grains at opposite corners of the sample domain with identical orientations, and (b) their local grain neighborhoods.

strain. We find the grain scale distributions to have means of 0.90%, 3.13%, 8.38%, and 11.95%, with standard deviations of 0.43%, 1.79%, 3.60%, and 4.55% at 0.4%, 0.8%, 1.5%, and 4.0% macroscopic strain, respectively. We omit the figures as they do not change appreciably from the case of one boundary layer removed. Removing three layers of elements yields similar trends at the element and grain scales, and the results are omitted for sake of brevity. Domain scale statistics for the removal of one and two grain boundary layers are summarized in Table 6. Collectively, the data indicates that the elements residing at the grain boundaries have similar distributions as those interior to the grain, indicating that the rigid grain interaction does not have appreciable influence on the observed trends.

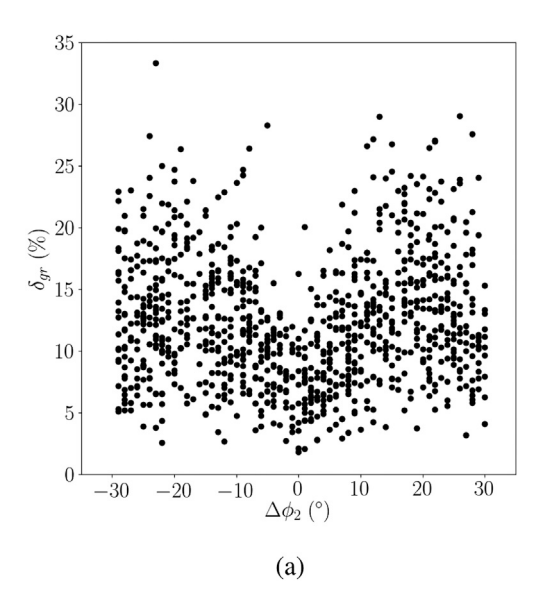
## 5.6. Orientations and grain neighborhoods

Finally, we inspect the trends regarding the influence of orientations and grain neighborhoods. To this end, we generate a reference sample that is a special case of that described in Section 3—i.e., a 1000-grain sample with random orientations. In this case, however, two grains at opposite corners of the mesh are chosen and given identical

**Table 6**Domain scale stress differences at the four macroscopic strain states of interest for analysis with element layers along the grain boundaries removed from consideration, for three levels of grain boundary layers removed.

2 Layers		
$\delta_{dom}$ (%)		
0.062		
0.358		
0.674		
0.514		

orientations. In the altered simulation, we apply the same rotation,  $\Delta\phi_2$ , about the c axis for these two grains, while the rest of the grains in the mesh are assigned random values of  $\Delta\phi_2$ , as before. In other words, these two grains share identical reference orientations and identical altered orientations, but their grain neighborhoods are both different in the reference sample and have varying degrees of rotation in the altered sample. We plot the grains and their neighborhoods from the reference simulation in Figs. 15(a) and (b), respectively. These samples (reference and altered) are used for the following analysis.



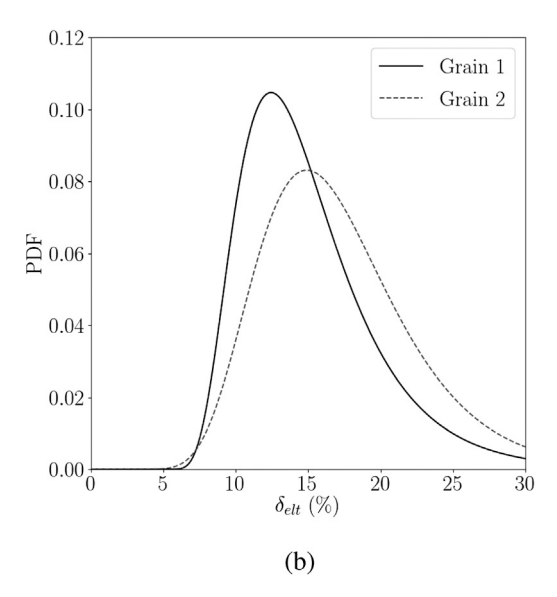


Fig. 16. (a) A depiction of the grain scale stress differences as a function of  $\Delta\phi_2$ , and (b) probability density functions for the two grains with identical reference and altered orientations (Fig. 15(a)), where Grain 1 has a mean of 15.06% and standard deviation of 4.59%, and grain 2 has a mean of 17.18% and a standard deviation of 5.55%. Both plots depict data at 4% macroscopic strain.

First, we inspect the differences,  $\delta_{gr}$ , as a function of  $\Delta\phi_2$  in an effort to illuminate potential orientation effects. We find that there is a propensity for grains with a higher  $\Delta\phi_2$  to exhibit a larger difference at the grain scale, as shown in Fig. 16(a), which depicts data at a macroscopic strain of  $\epsilon=4\%$ . Generally, when  $\Delta\phi_2$  is low,  $\delta_{gr}$  has lower magnitude than when  $\Delta\phi_2$  approaches  $\pm 30^\circ$ , indicating a positive correlation between the difference in rotation about the c axis with difference in stress state. However, there are relatively wide spreads in data. Even at  $\Delta\phi_2=0$ ,  $\delta_{gr}$  ranges from approximately 2.5% to greater than 10%, while at  $\Delta\phi_2=\pm 30$  this range is approximately 5% to 30%. This indicates, broadly, neighborhood effects.

To further understand the effects of orientation and neighborhood, we inspect Fig. 16(b), which depicts lognormal fits to the elemental differences,  $\delta_{elt}$ , for the two grains of interest in Fig. 15(a) at a macroscopic strain of  $\epsilon=4\%$ . Here, the distributions have similar character, but with noticeable differences. Namely, their means show non-negligible difference—15.06% compared to 17.18%—as well as their standard deviations—4.59% compared to 5.55%, respectively. If  $\delta_{elt}$  was entirely influenced by orientation alone, we would expect these curves to perfectly overlap, as the grains share identical reference and altered orientations. While the distributions are relatively close – indeed indicating an influence of orientation – the appreciable degree of difference between the curves indicates a strong influence of neighboring grains.

### 6. Conclusion

We have presented a study probing the consequences of orientation ambiguity in polarized light microscopy (PLM) characterization when utilized as a tool to inform virtual polycrystals in crystal plasticity finite element simulations. An idealized microstructure was developed to serve as a reference simulation, from which random c-axis-similar samples were generated. We performed deformation simulations on each sample, applying identical deformation histories, and the stress fields were compared to assess PLM's applicability to CPFEM deformation modeling. Overall, simulation results reveal:

 In the elastic regime, the stress predictions between the reference simulation and the altered simulations compare to an acceptable degree, often with a mean difference of less than 5%. This is attributed to the transverse isotropic elastic nature of HCP crystals. However, as crystallographic slip becomes more prevalent across

- the domain of the sample (i.e., through the elastic-plastic transition), the stress field predictions in the altered simulations deviate considerably from the predictions of the reference simulation.
- The character of the distributions of stress differences is affected by the scale being considered. At the element scale, the difference distributions had both the highest means and standard deviations. At the grain scale, we observe that the difference distributions exhibited noticeably smaller means and standard deviations (i.e., less deviation from the reference simulation). Finally, the domain scale consistently exhibited small differences (though this is somewhat attributed to the random texture considered in this study).
- There is no significant spatial correlation of differences in the stress predictions. When removing the grains along the control surface boundaries, grains along the free surfaces, or elements along grain boundaries from analysis, we do not observe an appreciable change in the distributions of stress differences.
- Both orientations and neighborhoods are observed to influence the differences observed between the altered and reference samples. Further study is necessary to fully explore this result, perhaps using novel graph-based methods [51].

Overall, the results indicate that PLM may have differing degrees of applicability at different scales for consideration (and thus different predictions). At the element scale (i.e., intragrain), the ambiguity in the rotation about the c axis leads to relatively large differences in stress predictions. Models or predictions that rely on local values (e.g., fatigue or fracture) may find such degrees of variability unacceptable. As the scale is increased to the grain scale, the results become somewhat more acceptable, which could (for example) serve to help inform methods such as HEXRD, which returns grain-averaged results. Domain scale, or macroscopic results, tend to give acceptable predictions, though further study is necessary regarding the influence of texture and other aspects.

Finally, we again note that the limitations of this study – primarily the inspection of an equiaxed, randomly textured sample subjected to monotonic loading – were important to provide first insight into consequences of PLM orientation ambiguity on CPFEM predictions, but leave a wide swath of parameter space untouched. Further study is necessary to understand the effects of these simulation parameters. As such, we are not confident in a complete understanding of behavior, and reserve suggestion regarding whether CPFEM simulations can unequivocally be informed by PLM characterization, or how to choose the full orientation if PLM is to be used.

#### Declaration of competing interest

The authors declare that they have no known competing financial interests or personal relationships that could have appeared to influence the work reported in this paper.

## Acknowledgments

The authors would like to thank Dr. Romain Quey for development of Neper, the capabilities of which were necessary for this study. We thank Ezra Mengiste for persistent support with scripting and plotting. LvW and MK were funded or partially funded by Air Force Research Laboratory, United States Grant FA8650-20-D-5211. AS was funded by the National Science Foundation, United States through award DMR-2143808. MO, PS, and TT acknowledge funding from the Air Force Research Laboratory, United States.

#### References

- G. Sachs, Zur ableitung einer fliessbedingung, Z. Ver. Dtsch. Ing. 72 (1928) 734–736.
- [2] G.I. Taylor, Plastic strain in metals, J. Inst. Met. 62 (1938) 307-324.
- [3] E. Kröner, On the plastic deformation of polycrystals, Acta Metall. 9 (2) (1961)
- [4] R. Lebensohn, C. Tomé, A self-consistent anisotropic approach for the simulation of plastic deformation and texture development of polycrystals: Application to zirconium alloys, Acta Metall. Mater. 41 (9) (1993) 2611–2624, http://dx.doi. org/10.1016/0956-7151(93)90130-K.
- [5] E. Marin, P. Dawson, On modelling the elasto-viscoplastic response of metals using polycrystal plasticity, Comput. Methods Appl. Mech. Engrg. 165 (1) (1998) 1–21, http://dx.doi.org/10.1016/S0045-7825(98)00034-6.
- [6] E. Marin, P. Dawson, Elastoplastic finite element analyses of metal deformations using polycrystal constitutive models, Comput. Methods Appl. Mech. Engrg. 165 (1) (1998) 23–41, http://dx.doi.org/10.1016/S0045-7825(98)00033-4.
- [7] F. Roters, P. Eisenlohr, L. Hantcherli, D. Tjahjanto, T. Bieler, D. Raabe, Overview of constitutive laws, kinematics, homogenization and multiscale methods in crystal plasticity finite-element modeling: Theory, experiments, applications, Acta Mater. 58 (4) (2010) 1152–1211, http://dx.doi.org/10.1016/j.actamat.2009.10. 058.
- [8] N.R. Council, Integrated Computational Materials Engineering: A Transformational Discipline for Improved Competitiveness and National Security, The National Academies Press, Washington, DC, 2008, http://dx.doi.org/10.17226/ 12199
- K. Chatterjee, M.P. Echlin, M. Kasemer, P.G. Callahan, T.M. Pollock, P. Dawson, Prediction of tensile stiffness and strength of Ti-6Al-4V using instantiated volume elements and crystal plasticity, Acta Mater. 157 (2018) 21–32, http://dx.doi.org/ 10.1016/j.actamat.2018.07.011.
- [10] M. Horstemeyer, Integrated Computational Materials Engineering (ICME) for Metals: Concepts and Case Studies, Wiley, 2018.
- [11] W. Soffa, D. Laughlin, High-strength age hardening copper-titanium alloys: redivivus, Prog. Mater. Sci. 49 (3) (2004) 347–366, http://dx.doi.org/10.1016/ S0079-6425(03)00029-X, A Festschrift in Honor of T. B. Massalski.
- [12] A. Suzuki, T.M. Pollock, High-temperature strength and deformation of γ/γ' two-phase Co–Al–W-base alloys, Acta Mater. 56 (6) (2008) 1288–1297, http://dx.doi.org/10.1016/j.actamat.2007.11.014.
- [13] M. Komarasamy, K. Alagarsamy, L. Ely, R.S. Mishra, Characterization of 3" through-thickness friction stir welded 7050-T7451 Al alloy, Mater. Sci. Eng. A 716 (2018) 55–62, http://dx.doi.org/10.1016/j.msea.2018.01.026.
- [14] B.L. Adams, S.I. Wright, K. Kunze, Orientation imaging: The emergence of new microscopy, Metall. Trans. A 24 (4) (1993) 819–831, http://dx.doi.org/10.1007/ PRO06E6602
- [15] A.J. Wilkinson, T.B. Britton, Strains, planes, and EBSD in materials science, Mater. Today 15 (9) (2012) 366–376, http://dx.doi.org/10.1016/S1369-7021(12)70163-3.
- [16] N. Brodusch, M. Trudeau, P. Michaud, L. Rodrigue, J. Boselli, R. Gauvin, Contribution of a new generation field-emission scanning electron microscope in the understanding of a 2099 Al-Li alloy, Microsc. Microanal. 18 (6) (2012) 1393–1409, http://dx.doi.org/10.1017/S143192761200150X.
- [17] H. Poulsen, Three-Dimensional X-Ray Diffraction Microscopy: Mapping Polycrystals and their Dynamics, in: Springer Tracts in Modern Physics, Springer Berlin Heidelberg, 2004.
- [18] J.C. Schuren, P.A. Shade, J.V. Bernier, S.F. Li, B. Blank, J. Lind, P. Kenesei, U. Lienert, R.M. Suter, T.J. Turner, D.M. Dimiduk, J. Almer, New opportunities for quantitative tracking of polycrystal responses in three dimensions, Curr. Opin. Solid State Mater. Sci. 19 (4) (2015) 235–244, http://dx.doi.org/10.1016/j.cossms.2014.11.003, Opportunities in Mesoscale Science.

- [19] R. Pokharel, J. Lind, S.F. Li, P. Kenesei, R.A. Lebensohn, R.M. Suter, A.D. Rollett, In-situ observation of bulk 3D grain evolution during plastic deformation in polycrystalline Cu, Int. J. Plast. 67 (2015) 217–234, http://dx.doi.org/10.1016/ j.iiplas.2014.10.013.
- [20] J. He, D. Borisov, J.D. Fleming, M. Kasemer, Subsurface polycrystalline reconstruction based on full waveform inversion A 2D numerical study, Materialia 24 (2022) 101482, http://dx.doi.org/10.1016/j.mtla.2022.101482.
- [21] B. Lan, T. Ben Britton, T.-S. Jun, W. Gan, M. Hofmann, F.P. Dunne, M.J. Lowe, Direct volumetric measurement of crystallographic texture using acoustic waves, Acta Mater. 159 (2018) 384–394, http://dx.doi.org/10.1016/j.actamat.2018.08.
- [22] P. Dryburgh, R.J. Smith, P. Marrow, S.J. Lainé, S.D. Sharples, M. Clark, W. Li, Determining the crystallographic orientation of hexagonal crystal structure materials with surface acoustic wave velocity measurements, Ultrasonics 108 (2020) 106171, http://dx.doi.org/10.1016/j.ultras.2020.106171.
- [23] Y. Liu, M.K. Kalkowski, M. Huang, M.J. Lowe, V. Samaitis, V. Cicènas, A. Schumm, Can ultrasound attenuation measurement be used to characterise grain statistics in castings? Ultrasonics 115 (2021) 106441, http://dx.doi.org/10.1016/j.ultras.2021.106441.
- [24] L. Böhme, L. Morales-Rivas, S. Diederichs, E. Kerscher, Crystal c-axis mapping of hcp metals by conventional reflected polarized light microscopy: Application to untextured and textured cp-Titanium, Mater. Charact. 145 (2018) 573–581, http://dx.doi.org/10.1016/j.matchar.2018.09.024.
- [25] K.-W. Jin, M. De Graef, c-Axis orientation determination of α-titanium using Computational Polarized Light Microscopy, Mater. Charact. 167 (2020) 110503, http://dx.doi.org/10.1016/j.matchar.2020.110503.
- [26] K.-W. Jin, M. De Graef, Correlation of c-axis orientation of a-titanium grains with polarized light optical microscopy intensity profiles, Microsc. Microanal. 24 (S1) (2018) 548–549, http://dx.doi.org/10.1017/S1431927618003239.
- [27] X. Wang, S. Yang, M. Seita, Combining polarized light microscopy with machine learning to map crystallographic textures on cubic metals, Mater. Charact. 190 (2022) 112082, http://dx.doi.org/10.1016/j.matchar.2022.112082, URL https://www.sciencedirect.com/science/article/pii/S1044580322003643.
- [28] TiPolar, Optical microscope for orientation imaging, 2023, Accessed on June 9, 2023. URL https://www.tipolar.com/.
- [29] D. Rowenhorst, A.D. Rollett, G.S. Rohrer, M. Groeber, M. Jackson, P.J. Konijnenberg, M.D. Graef, Consistent representations of and conversions between 3D rotations, Modelling Simul. Mater. Sci. Eng. 23 (8) (2015) 083501, http://dx.doi.org/10.1088/0965-0393/23/8/083501.
- [30] N.R. Barton, D.E. Boyce, P.R. Dawson, Pole figure inversion using finite elements over rodrigues space, Textures Microstruct. 35 (2) (2002) 113–144, http://dx. doi.org/10.1080/073033002100000182.
- [31] E. Wielewski, D.E. Boyce, J.-S. Park, M.P. Miller, P.R. Dawson, A methodology to determine the elastic moduli of crystals by matching experimental and simulated lattice strain pole figures using discrete harmonics, Acta Mater. 126 (2017) 469–480, http://dx.doi.org/10.1016/j.actamat.2016.12.026.
- [32] M. Kasemer, M.P. Echlin, J.C. Stinville, T.M. Pollock, P. Dawson, On slip initiation in equiaxed  $\alpha/\beta$  Ti-6Al-4V, Acta Mater. 136 (2017) 288–302, http://dx.doi.org/10.1016/j.actamat.2017.06.059.
- [33] F. Azhari, W. Davids, H. Chen, S.P. Ringer, C. Wallbrink, Z. Sterjovski, B.R. Crawford, D. Agius, C.H. Wang, G. Schaffer, A comparison of statistically equivalent and realistic microstructural representative volume elements for crystal plasticity models, Integr. Mater. Manuf. Innov. 11 (2) (2022) 214–229, http://dx.doi.org/10.1007/s40192-022-00257-4.
- [34] J. Cappola, J.-C. Stinville, M.-A. Charpagne, P.G. Callahan, M.P. Echlin, T.M. Pollock, A. Pilchak, M. Kasemer, On the localization of plastic strain in microtextured regions of Ti-6Al-4V, Acta Mater. 204 (2021) 116492, http://dx.doi.org/10.1016/j.actamat.2020.116492.
- [35] J. Takahashi, H. Suito, Evaluation of the accuracy of the three-dimensional size distribution estimated from the schwartz-saltykov method, Metall. Mater. Trans. A 34 (1) (2003) 171–181, http://dx.doi.org/10.1007/s11661-003-0218-6.
- [36] D.M. Turner, S.R. Kalidindi, Statistical construction of 3-D microstructures from 2-D exemplars collected on oblique sections, Acta Mater. 102 (2016) 136–148, http://dx.doi.org/10.1016/j.actamat.2015.09.011.
- [37] I. Javaheri, V. Sundararaghavan, Polycrystalline microstructure reconstruction using Markov random fields and histogram matching, Comput. Aided Des. 120 (2020) 102806, http://dx.doi.org/10.1016/j.cad.2019.102806.
- [38] P. Acar, A. Ramazani, V. Sundararaghavan, Crystal plasticity modeling and experimental validation with an orientation distribution function for Ti-7Al alloy, Metals 7 (11) (2017) http://dx.doi.org/10.3390/met7110459.
- [39] M.P. Echlin, M. Kasemer, K. Chatterjee, D. Boyce, J.C. Stinville, P.G. Callahan, E. Wielewski, J.-S. Park, J.C. Williams, R.M. Suter, T.M. Pollock, M.P. Miller, P.R. Dawson, Microstructure-based estimation of strength and ductility distributions for  $\alpha + \beta$  titanium alloys, Metall. Mater. Trans. A 52 (6) (2021) 2411–2434.
- [40] M. Kasemer, G. Falkinger, F. Roters, A numerical study of the influence of crystal plasticity modeling parameters on the plastic anisotropy of rolled aluminum sheet, Modelling Simul. Mater. Sci. Eng. 28 (8) (2020) 085005, http://dx.doi. org/10.1088/1361-651X/abb8e2.
- [41] P.R. Dawson, D.E. Boyce, FEpX Finite Element Polycrystals: Theory, finite element formulation, numerical implementation and illustrative examples, 2015, arXiv:arXiv:1504.03296.

[42] R. Quey, M. Kasemer, The Neper/FEPX project: Free / open-source polycrystal generation, deformation simulation, and post-processing, IOP Conf. Ser.: Mater. Sci. Eng. 1249 (1) (2022) 012021, http://dx.doi.org/10.1088/1757-899x/1249/ 1/012021.

L. van Wees et al.

- [43] R. Quey, P. Dawson, F. Barbe, Large-scale 3D random polycrystals for the finite element method: Generation, meshing and remeshing, Comput. Methods Appl. Mech. Engrg. 200 (17–20) (2011) 1729–1745, http://dx.doi.org/10.1016/j.cma. 2011.01.002
- [44] J.F. Nye, Physical Properties of Crystals, in: Oxford Science Publications, Oxford University Press, London, England, 1957.
- [45] S. Nemat-Nasser, M. Obata, Rate-dependent, finite elasto-plastic deformation of polycrystals, Proc. R. Soc. Lond. Ser. A Math. Phys. Eng. Sci. 407 (1833) (1986) 343–375.
- [46] M.P. Echlin, J.C. Stinville, V.M. Miller, W.C. Lenthe, T.M. Pollock, Incipient slip and long range plastic strain localization in microtextured Ti-6Al-4V titanium, Acta Mater. 114 (2016) 164–175, http://dx.doi.org/10.1016/j.actamat.2016.04. 057.
- [47] M. Kasemer, P. Dawson, A finite element methodology to incorporate kinematic activation of discrete deformation twins in a crystal plasticity framework, Comput. Methods Appl. Mech. Engrg. 358 (2020) 112653, http://dx.doi.org/ 10.1016/j.cma.2019.112653.
- [48] M. Kasemer, Finite element polycrystal plasticity, 2023, Accessed on May 24, 2023. URL http://fepx.info.
- [49] W. Hosford, The Mechanics of Crystals and Textured Polycrystals, in: Oxford Engineering Science Series, Oxford University Press, 1993.
- [50] A. Bower, Applied Mechanics of Solids, CRC Press, 2009.
- [51] D.C. Pagan, C.R. Pash, A.R. Benson, M.P. Kasemer, Graph neural network modeling of grain-scale anisotropic elastic behavior using simulated and measured microscale data, npj Comput. Mater. 8 (1) (2022) http://dx.doi.org/10.1038/s41524-022-00952-y.